Influence of large biased surfaces on the plasma parameters in the extraction region of a negative hydrogen ion source

Dimitar Yordanov, Dirk Wünderlich, Christian Wimmer, Ursel Fantz, Dominikus Pius Zielke

Angaben zur Veröffentlichung / Publication details:

Yordanov, Dimitar, Dirk Wünderlich, Christian Wimmer, Ursel Fantz, and Dominikus Pius Zielke. 2025. "Influence of large biased surfaces on the plasma parameters in the extraction region of a negative hydrogen ion source." *Plasma Sources Science and Technology* 34 (8): 085011. https://doi.org/10.1088/1361-6595/adf7d4.

Influence of large biased surfaces on the plasma parameters in the extraction region of a negative hydrogen ion source

OPEN ACCESS
IOP Publishing
Plasma Sources Science and Technology
Plasma Sources Sci. Technol. **34** (2025) 085011 (14pp)
https://doi.org/10.1088/1361-6595/adf7d4

Influence of large biased surfaces on the plasma parameters in the extraction region of a negative hydrogen ion source

D Yordanov[1,*], **D Wünderlich**[1], **C Wimmer**[1], **U Fantz**[1,2] and **D Zielke**[1]

[1] Max-Planck-Institut für Plasmaphysik, Boltzmannstr. 2, 85748 Garching, Germany
[2] AG Experimentelle Plasmaphysik Universität Augsburg, 86135 Augsburg, Germany

E-mail: dimitar.yordanov@ipp.mpg.de

Received 3 December 2024, revised 7 July 2025
Accepted for publication 5 August 2025
Published 14 August 2025

Abstract

The neutral beam injection system in the upcoming fusion reactor ITER will use radio-frequency (RF), low-pressure, and high-power negative hydrogen/deuterium ion plasma sources. The extraction of negative ions from the plasma is always accompanied by co-extraction of undesirable electrons, which can limit the source performance. This paper aims to investigate the effect of biased surfaces in the vicinity of the extraction on the plasma parameters towards the reduction of the co-extracted electrons. For this purpose, a 2D fluid plasma model is employed on a prototype plasma ion source where the biases of two different surfaces are varied independently. Since self-consistent RF fluid plasma models can be computationally heavy and time-demanding, the study of the effect of biased surfaces uses a simplified model where the RF heating is replaced with a power deposition profile, set as an input parameter. This procedure reduces the degree of freedom by more than one order of magnitude and, respectively, the computational time from tens of hours to several for one run of the model. To justify the method, the simplified model is first compared with a benchmarked RF self-consistent model on a smaller geometry. Both models produce similar results for the plasma parameters in the region of interest, namely, close to the extraction, which gives the confidence to use the simplified model for the purpose of the study. Applying a positive bias to large surfaces in the vicinity of the extraction region provides a higher electron density and plasma potential as well as a change in the electron flux orientation. However, the difference between the surface and the plasma potentials decreases more than two times and in combination with the reversed orientation of the flux, the electron current collected by the biased

* Author to whom any correspondence should be addressed.

electrodes increases. The modelling results for the currents collected by the biased surfaces indicate similar behaviour to the experimental ones.

Keywords: negative ion source, biased surfaces, fluid plasma modelling

1. Introduction

Plasma sources have a wide range of applications in the industry [1] and medicine [2], but they are also being used as charged particle sources for accelerators [3] and neutral beam injection (NBI) heating systems in fusion reactors [4]. The upcoming fusion experiment ITER will require a neutral beam with a current density of 230 Am^{-2} accelerated to 870 keV for hydrogen and 200 Am^{-2} with 1 MeV for deuterium and beam uniformity to be better than 90% [5, 6]. However, at these high energies, the neutralisation of the positive hydrogen/deuterium ions is not efficient [7]; thus, the use of negative ions is mandatory. The foreseen negative ion source for ITER NBI is based on (1) the radio-frequency (RF), two-chamber prototype ion source at the BUG (Bavarian test machine for negative ions UpGrade) test facility [8] at the Max Planck Institute in Garching, Germany.

An inductively coupled cylindrical coil ignites and sustains the discharge in a driver (a quartz tube with a Faraday screen) followed by expanding plasma in a second larger metal chamber where the extraction system is located, opposite to the driver (figure 1). The extracted negative ions are produced mainly by the conversion of atoms on a surface with a low work function (≈ 1.4 eV), typically on the first grid of the extraction system. The low work function is achieved by adding a small amount of caesium vapour in the source [9]. To reduce the negative ion losses by electron collisions (electron affinity of the hydrogen/deuterium is 0.75 eV), the electron temperature (T_e) is lowered by applying a magnetic filter field (MFF) strong enough to magnetise the electrons, but not the ions (20–60) G. The ion source is equipped with an extraction system, containing a plasma grid (PG) in contact with the plasma, an extraction grid (EG) with embedded magnets for deflection of the electrons from the extracted beam and an acceleration grid. Each grid has many extraction apertures arranged in beamlet groups. A window-frame-structured bias plate (BP) is placed in front of the PG, allowing the plasma to reach only the beamlet groups. Furthermore, the working filling pressure is required to be 0.3 Pa or less to minimise the stripping losses of the beam in the accelerator.

The magnetic field ($\mathbf{B}_{FF}$) in the expansion of the source ensures an axial drop of T_e to ≈ 1 eV and of the electron density (n_e) [10] with one order of magnitude in the region and provides an initial decrease of the co-extracted electron current. The strong T_e and n_e gradients create a diamagnetic drift and, together with the $\mathbf{E} \times \mathbf{B}_{FF}$ drift, are the main contributors in the electron momentum balance equation. The resulting electron flux ($\mathbf{\Gamma}_e$) in the vertical direction has a vortex-type structure and provides an off-axis accumulation of electrons in the region of the MFF [11]. This leads to a strong vertical asymmetry of the co-extracted electrons and localised power deposition on the EG and limit the source performance.

While BUG has one driver, the full-scale ion source for ITER, SPIDER (Source for Production of Ion of Deuterium Extracted from RF plasma) [12] at Consorzio RFX in Padua, Italy, has eight drivers and, respectively, a bigger expansion chamber. On the other hand, the ion source at the ELISE (Extraction from a Large Ion Source Experiment) test facility [13] at the Max Planck Institute in Garching, Germany, is an intermediate step in the preparation of the ITER NBI source. It is half the size of SPIDER and intends to meet ITER requirements [14] concerning negative ion and electron current densities and their ratio being below 1, achieving good beam homogeneity and formulating operational scenarios. However, reducing and stabilising the co-extracted electron current is a challenging task, it remains high even with already applied MFF, particularly at high RF power ($\leqslant 50$ kW/driver) and high extraction and accelerating voltages. In addition, for long pulse extraction the co-extracted electron current increases over time, particularly in deuterium, making the task more challenging. In the standard operation, the amount of co-extracted electrons is reduced by a positive bias applied to the PG [15] with respect to the source body and the BP. Particle-in-cell codes with Monte Carlo collisions [10, 16] indicate that this effect could be due to the collection of plasma electrons by the PG surface. However, an alternative biasing technique by biasing simultaneously the PG and letting the BP on a floating potential, experimentally tested at ELISE, shows further decrease and symmetrise of the co-extracted electrons [17, 18]. However, the experimental diagnostic methods (Langmuir probes, optical emission spectroscopy and cavity ring-down spectroscopy) are at fixed locations and measure the plasma properties locally; hence, global effects cannot be studied easily.

A fluid plasma model [19, 20] is employed on the 2D geometry of the ELISE ion source for the first time to investigate the plasma overlap of the drivers, its uniformity in the vicinity of the large extraction area and to study the underlying physics principles at different potentials applied to the PG and the BP simultaneously, which can lead to optimising the co-extracted electron current density.

The modelling within the fluid plasma approach is based on the particle and the energy fluxes and can be applied to simulate the plasma properties in the presence of MFF [11, 21]. For complicity, the fluid plasma equations can be coupled with the Maxwell equations to account for the RF coil and respectively, the RF electromagnetic fields, igniting and sustaining the discharge [22, 23]. Unfortunately, reaching a quasi-steady state of the discharge usually takes up to 0.1 s, with a typical RF time scale of μs, it would take an unreasonable calculation

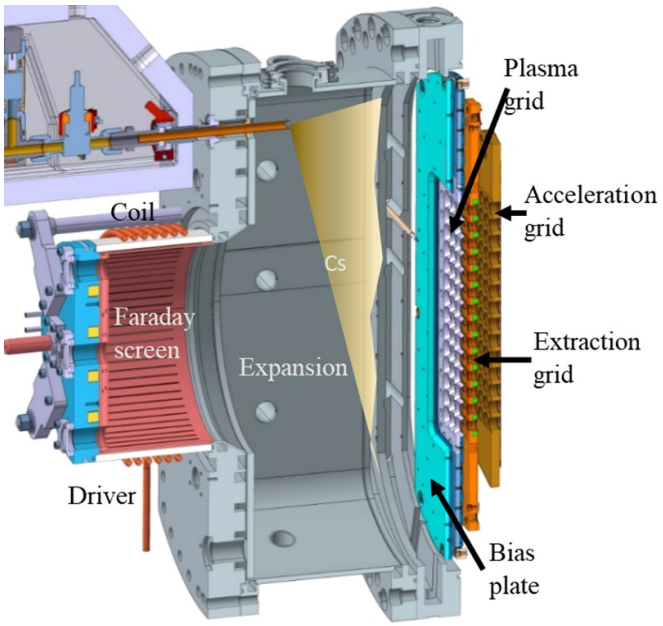

Figure 1. CAD drawing of the ion source at the BUG test facility.

time. Using the time-harmonic approximation of the Maxwell equation reduces the calculation time to tens of hours for one model run. However, the intention of this paper is to study the effect of PG and BP bias on the plasma parameters in the vicinity of the extraction at ELISE, therefore, variations of the PG and BP potentials would take a lot of computational time. To reduce the calculation time, first in section 3 , the results are compared with the BUG geometry from a well-studied and benchmarked RF self-consistent fluid plasma model [20] applied in Cartesian coordinates with a simplified model. The latter does not take into account the coil, but uses a power deposition profile as an input parameter, obtained from the full model. The self-consistent model can resolve the change of the plasma parameters over the RF cycle, showing the well-known fluctuation of the plasma potential, which also affects the electron flux. Comparing the results from both models indicates differences in the plasma parameters in the driver region but similar behaviour in the expansion. This outcome justifies the use of the simplified model in the ELISE geometry to study the PG and BP bias effects on the plasma properties in the vicinity of the extraction region in section 4. The extraction of the negative ions and the co-electrons requires the coupling to an extraction code [24], which is out of the scope of this study.

2. Description of the model

2.1. BUG modelling domain

The RF prototype ion source at the BUG test facility has a cylindrical driver where the plasma is generated and expands towards the extraction system in a larger chamber (figure 1). The modelling domain with the real size of BUG is a 2D vertical (y–z) planar plane, taken in the middle ($x = 0$ m) of

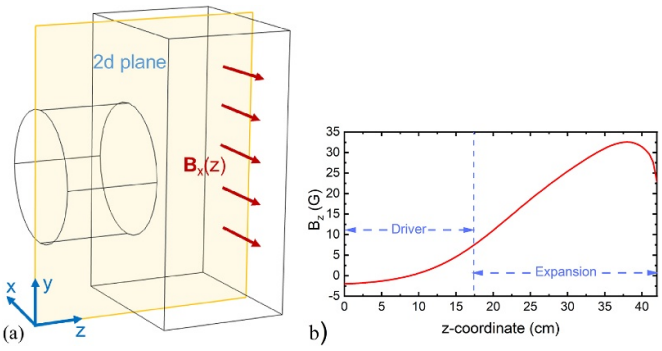

Figure 2. Schematic representation of the BUG ion source (a) and the axial profile of MFF used in the calculations (b).

the driver (figure 2(a)). The calculations are made with an MFF ($\mathbf{B}_{\rm FF} = (B_x(z), 0, 0)$) with a direction perpendicular to the modelling plane. The axial profile of $\mathbf{B}_{\rm FF}$ is the same as the one used in experiments, figure (2(b)), where the magnetic field is produced by high-current flowing through the PG ($I_{\rm PG} = 1.5$ kA with a maximum of $\mathbf{B}_{\rm FF} = 32$ G, located 3 cm away from the PG). The magnetic field breaks the axial symmetry due to $\mathbf{E} \times \mathbf{B}_{\rm FF}$ and diamagnetic particle drifts, leading to a vertical asymmetry of the plasma parameters [10, 11] and therefore, the model is employed in a planar plane with Cartesian coordinates.

2.2. Gas-discharge part of the model

The model is within the fluid plasma theory and it is based on [19] and [20], where the initial set of equations includes the particle balance equations for electrons ($\alpha = $ e) and the positive hydrogen ions ($\alpha = $ i, where i = 1, 2 and 3 for the H^+, H_2^+ and H_3^+ ions)

$$\partial_t n_\alpha + \nabla \cdot n_\alpha \mathbf{v}_\alpha = \mathcal{R}_\alpha, \tag{1}$$

the electron energy balance equation

$$\partial_t \left(\frac{3}{2} e n_{\rm e} T_{\rm e} \right) + \nabla \cdot \mathbf{Q}_{\rm e} = P_{\rm ind} + e n_{\rm e} \mathbf{v}_{\rm e} \cdot \nabla \Phi - P_{\rm e} \tag{2}$$

and the Poisson equation

$$\nabla^2 \Phi = -\frac{e}{\epsilon_0} \left(\sum_{i=1}^{3} n_{\rm i} - n_{\rm e} \right). \tag{3}$$

In the equations (1)–(3): n_α, $\mathbf{v}_\alpha$ and $\mathcal{R}_\alpha$ are respectively the density, the velocity and the production-loss rate of the particles; $T_{\rm e}$ is the electron temperature, defined as the mean thermal energy, since the electrons are assumed to be with Maxwell distribution; $\mathbf{Q}_{\rm e}$ is the electron energy flux; $P_{\rm ind}$ and $P_{\rm e}$ are inductive heating power and electron energy losses in collisions; Φ is the plasma potential of the electrostatic plasma field $\mathbf{E} = -\nabla_{(y,z)} \Phi$ formed due to the charged particle fluxes to the discharge walls; ϵ_0 and e are the vacuum permittivity and electron elementary charge respectively.

The mesh is triangular in the modelling domain and rectangular on the walls. The mesh size varies from 0.1 mm near the walls to 1 mm in the volume, and the typical Debye length is in the order of 1 μm, which is 100 times smaller than the minimum mesh size. The Poisson equation (3) is converted into a weak form, and in combination with the finite element method, the solution is approximated via Lagrange shape functions. After that, the solver iteratively refines this solution, ensuring it satisfies the equation and the specified Dirichlet boundary conditions. The formed sheath [22] extends over a few grid cells in front of the wall, and it has the correct steady-state potential drop for electrons in Boltzmann equilibrium [25]. In addition, the sheath correctly describes the potential locking when an additional large surface is biased to a higher potential with respect to the source walls [26]. The latter effect will be discussed in more detail in section 4.2.2.

The particle velocity $\mathbf{v}_\alpha$ is obtained from the momentum balance equation:

$$\begin{aligned} & m_\alpha n_\alpha \left[\partial_t \mathbf{v}_\alpha + (\mathbf{v}_\alpha \cdot \nabla)\,\mathbf{v}_\alpha\right] \\ & \quad = Z_\alpha n_\alpha e\left(-\mathbf{E} + \mathbf{v}_\alpha \times \mathbf{B}\right) \\ & \qquad - m_\alpha n_\alpha \nu_{\alpha,\mathrm{n}} \mathbf{v}_\alpha - \nabla n_\alpha e T_\alpha - \nabla . \widehat{\pi_\alpha} \end{aligned} \tag{4}$$

where m_α and $\nu_{\alpha,\mathrm{n}}$ are the mass of the particle and the collision frequency of the charged particle with neutrals (atoms and molecules), Z_α indicate the sign of the charged particle ('+' for $\alpha =$ positively and '-' for negatively charged particles), $\mathbf{E}$ and $\mathbf{B}$ are electric and magnetic fields, respectively and $\widehat{\pi_\alpha}$ is the stress tensor. The divergence of the stress tensor is simplified to:

$$\nabla . \widehat{\pi_\alpha} = -m_\alpha n_\alpha \eta_\alpha \left[\nabla^2 \mathbf{v}_\alpha + \frac{1}{3}\nabla\left(\nabla . \mathbf{v}_\alpha\right)\right], \tag{5}$$

η_α is the viscosity. Since the calculations are at low pressure (0.3 Pa), the discharge is in a free-fall regime, and the advection term (the second term on the left-hand side of (4)) for the ions must not be neglected. In (2) the electron energy flux is

$$\mathbf{Q}_\mathrm{e} = \frac{5}{2} n_\mathrm{e} e T_\mathrm{e} \mathbf{v}_\mathrm{e} + \mathbf{q}_\mathrm{e} + \widehat{\pi}_\mathrm{e} \mathbf{v}_\mathrm{e} \tag{6}$$

where $\mathbf{q}_\mathrm{e}$ is the electron heat flux

$$\mathbf{q}_\mathrm{e} = -\frac{5}{2}\frac{n_\mathrm{e} e T_\mathrm{e}}{m_\mathrm{e}\nu_{\mathrm{e,n}}}\nabla e T_\mathrm{e} - \frac{e}{m_\mathrm{e}\nu_{\mathrm{e,n}}}\left(\mathbf{q}_\mathrm{e} \times \mathbf{B}\right). \tag{7}$$

The included reactions for creating and losses of charged particles are: ionisation of atoms, ionisation and dissociation of molecules, dissociation and dissociative recombination of molecular ions (H_2^+ and H_3^+). The corresponding rate coefficients are taken from [27]. The boundary conditions are the same as in [19]. The neutral hydrogen species are taken into account as a constant background over the modelling domain, with a molecular density of $2.5 \times 10^{19}\,\mathrm{m}^{-3}$ which is twice higher than the atomic density [20, 28], resulting in a pressure of 0.3 Pa. The dynamics of the neutrals are not accounted for as they are not within the scope of the study. The neutral and positive ion caesium dynamics and the effects related to it, such as collisions and sheath modifications, are not taken into account.

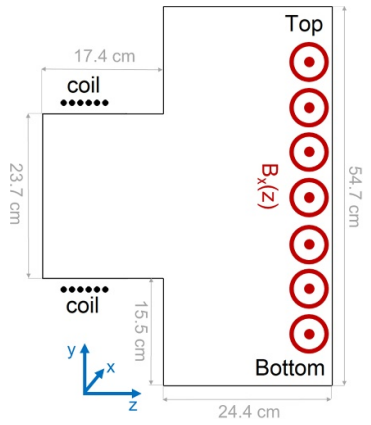

Figure 3. BUG ion source 2D modelling domain with the coil and the orientation of the magnetic filter field, used for the RF self-consistent model.

2.3. RF power coupling and power deposition profile

In the first step of the study, the model is solved by taking into account self-consistent RF power deposition into the discharge. Therefore, Ampere–Maxwell's law and Faraday's law of induction are solved for the RF electromagnetic fields ($\mathbf{E}_\mathrm{RF}$ and $\mathbf{B}_\mathrm{RF}$) and plasma current density ($\mathbf{J}_\mathrm{RF}$):

$$\nabla \times \mathbf{B}_\mathrm{RF} = \mu_0 \mathbf{J}_\mathrm{RF} \tag{8}$$

$$\nabla \times \mathbf{E}_\mathrm{RF} = -\partial_t \mathbf{B}_\mathrm{RF}. \tag{9}$$

In equation (8) the displacement current is neglected. The modelling domain includes the 6-turn coil with a wire diameter $d_\mathrm{coil} = 6$ mm, placed 12 mm from the driver wall (figure 3). The RF system is excited by the coil current density $J_{\mathrm{coil},x} = I_\mathrm{coil}/\pi d_\mathrm{coil}\sin(\omega t)$ over the coil circumference (similar to the skin depth of a copper conductor), where I_coil is the coil set current and $\omega = 2\pi f_0$ is the angular frequency at the driving frequency $f_0 = 1$ MHz. Since $J_{\mathrm{coil},x}$ is perpendicular to the modelling domain (y–z), the partial derivative in the x-direction is zero ($\partial_x = 0$), therefore the induced RF magnetic field ($\mathbf{B}_\mathrm{RF} = (0, B_{\mathrm{RF},y}, B_{\mathrm{RF},z})$) is parallel, and the RF electric field ($\mathbf{E}_\mathrm{RF} = (E_{\mathrm{RF},x}, 0, 0)$), as well as the plasma current density ($\mathbf{J}_\mathrm{RF} = (J_{\mathrm{RF},x}, 0, 0)$) are perpendicular to the modelling plane. Due to the higher mass of the ions compared to the electrons, only the electrons are heated directly by $\mathbf{E}_\mathrm{RF}$ [20].

The scope of the study is at a pressure of 0.3 Pa and an RF power (P_RF) of 60 kW, where the discharge is in the local skin regime [19, 20]. For a BUG operation with a set power on the generators of 60 kW requiring $I_\mathrm{coil} \approx 300$ A, providing a strong RF magnetic field $|B_\mathrm{RF}| > 200$ G at a maximum close to the side walls of the driver. Under these conditions, the RF Lorentz force ($\mathbf{F}_{\mathrm{L,RF}} = \mathbf{v}_\mathrm{e} \times \mathbf{B}_\mathrm{RF}$) in (equation (4)) for the electrons becomes comparable to the other forces. The electrons

are magnetised by B_{RF} and gyrate with a Larmor radius (of approximately 1 mm) on small orbits around the RF field lines and are transported through B_{RF} equipotential lines via collisions. The induced RF current density in the plasma is:

$$J_{\mathrm{RF},x} = -en_{\mathrm{e}}v_x, \tag{10}$$

depending on the electron velocity in the x-coordinate, which is perpendicular to the modelling domain. Therefore, equation (4) is decomposed into components and solved for v_x, v_y and v_z components. The x-component of the Lorentz force

$$(\mathbf{v}_{\mathrm{e}} \times \mathbf{B})_x = v_y B_z - v_z B_y \tag{11}$$

depends on the RF magnetic field components and (y–z) components of the velocity. Since $J_{\mathrm{coil},x}$ has a sinusoidal waveform $|B_{\mathrm{RF}}|$ oscillates from 0 to ≈ 200 A, affecting equation (10) and, respectively, the plasma conductivity. Since the calculations are with an MFF perpendicular to the modelling plane, the total magnetic field is a superposition of the RF and the filter fields. However, $\mathbf{B}_{\mathrm{FF}}$ is low in the driver ($\approx |2|$ G), and it is found that it has a negligible contribution to the RF electron dynamics and the formation of the inductive heating power profile:

$$P_{\mathrm{ind}} = \frac{1}{2}\mathrm{Re}\left\{J_{\mathbf{RF}}E_{\mathrm{RF}}\right\}. \tag{12}$$

The total absorbed RF power to the plasma is an integral of equation (12) over the discharge modelling plane. Additionally, the RF self-consistent model accounts for the network losses in the RF circuit (RF generators, Faraday screen and coil) and the absorbed RF power into the plasma is $\sim$60% of the set power.

Since the dynamics of the neutral hydrogen is not taken into account, it takes up to 40 RF cycles to reach a quasi-steady state for the charged particles in the RF self-consistent model, and this usually takes tens of hours. However, excluding the coil and respectively $\mathbf{J}_{\mathrm{RF}}$, $\mathbf{B}_{\mathrm{RF}}$ and $\mathbf{E}_{\mathrm{RF}}$ and all effects related to the RF and taking $P_{\mathrm{ind}}(y,z)$ in (2) as an input parameter, simplifies the model by providing at least one order of magnitude fewer degrees of freedom and respectively, the calculation time is reduced to several hours. In order to discuss the difference between both models, first the RF self-consistent model is solved and the obtained spatial distribution of $P_{\mathrm{ind}}(y,z)$ is imported to the simplified one. Both models are solved with the same parameters—pressure of 0.3 Pa and all walls are set to 0 V and 60 kW set power.

3. Results for BUG geometry

3.1. RF self-consistent model

Figure 4 shows the time-averaged over the RF period plasma parameters with a typical discharge structure at BUG with MFF [11, 29]. The electron flux (figure 4(a) the arrow plot) in a magnetic field is the result of the interplay between forces in (4), reflecting the vortex-type structure [11] and resulting in a vertical plasma asymmetry in the expansion [29]. Furthermore, the vortex structure of $\mathbf{\Gamma}_{\mathrm{e}}$, due to diamagnetic and $\mathbf{E}\times\mathbf{B}_{\mathrm{FF}}$ drifts, leads to the formation of a second smaller maxima of n_{e} and of Φ in the region with a high magnetic field. The vertical plasma inhomogeneity close to the PG can affect the co-extracted electron current top/bottom asymmetry: Φ changes from 24 V on top to 12 V on bottom and n_{e} from 1×10^{18} m^{-3} to 0.3×10^{18} m^{-3}. The first maxima of n_{e} located in the driver is squeezed in the area close to the coil due to the RF Lorentz and the ponderomotive forces pushing away the electrons from this region. On the other hand, the maximum of Φ in the driver is spreading to the wall next to the coil, despite the wall potential of 0 V. This is due to the RF component of the electric field (E_x). The maximum of T_{e} (figure 4(c)) is in the region of the coil, indicating electron heating with values of about 12 eV, followed by a radial decrease towards the middle of the driver. In the axial direction T_{e} reduces rapidly to values of (1–2) eV in the direct vicinity of the PG. As a consequence of the MFF, which penetrates into the driver, the first maxima of the plasma parameters (n_{e}, Φ and T_{e}) are not vertically (in y-direction) symmetric due to electron thermal flux (7) [11].

In an inductively coupled plasma, the plasma parameters of the discharge oscillate together with P_{RF} frequency ($2\omega_{\mathrm{RF}}$) and higher harmonics. Figure 5 shows the axial profile of the plasma parameters from the middle of the driver's backplate to the end of the modelling domain (the PG) for three different time moments within one oscillation, namely at the maximum, the middle and the minimum of the P_{RF} period. When the plasma is fully ignited and is in a quasi-stationary regime, the electron density oscillates around its averaged value, which is negligible (figure 5(a), changes are not visible in the figure—the lines overlap). The electron temperature varies from 8 to 9 eV in the driver within one oscillation (figure 5(b)). The MFF does not yet affect T_{e}, and the dominant processes are the ionisation due to electron energy gain within the RF period and loss via collisions. In the expansion, the MFF suppresses the electron heat flux, resulting in a strong reduction of T_{e} to below 2 eV, defining a region with a domination of the recombination processes, which is not affected by the RF heating. The electron temperature increase in the vicinity of the PG is due to the loss of electrons on the wall. The results for Φ show oscillation of the entire profile with more than 15 V (figure 5(c)) within one P_{RF} period. At the maximum of the P_{RF} period, the spatial distribution of Φ shows a region of high positive potential of 140 V close to the coil (figure 6(a)) however, the RF Lorentz and the ponderomotive forces restrict the electrons and their flux in this region. The electron flux (figure 6(a) the arrow plot) is similar to the averaged one (figure 4(a)): an intense flux towards the driver's backplate upstream of the expansion region. The formed vortex, associated with the diamagnetic drift caused by $\nabla(n_{\mathrm{e}}T_{\mathrm{e}})$, sends one part of the flux back to the driver's bottom side wall and another bigger part towards the expansion. The second vortex, associated with $\mathbf{E}\times\mathbf{B}_{\mathrm{FF}}$ drift, before the extraction region defines the orientation of $\mathbf{\Gamma}_{\mathrm{e}}$ in front of the PG—from bottom to top. In the middle of the P_{RF} period (figure 6(b)), the potential close to the coil tends to decrease, resulting in a shift of the entire Φ profile (figure 5(c) the red curve) to lower values, but in

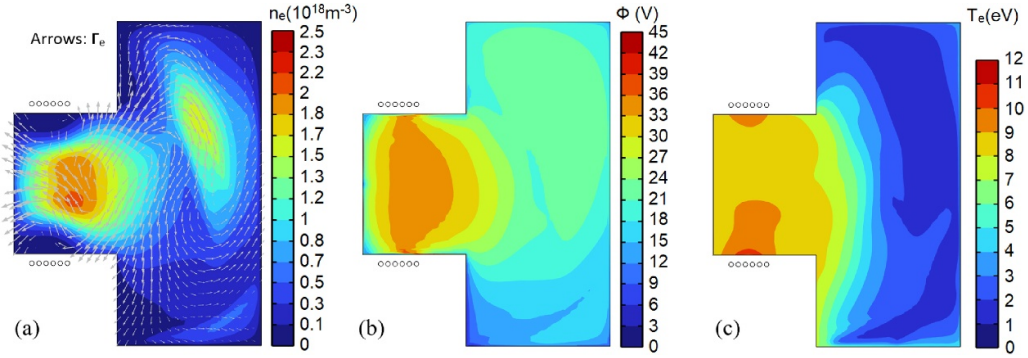

Figure 4. Time averaged over the RF cycle spatial distribution of the electron density and its flux with arrows (a), the plasma potential (b) and the electron temperature (c) obtained with MFF, pressure of 0.3 Pa and 60 kW of set RF power. The RF power is taken into account self-consistently.

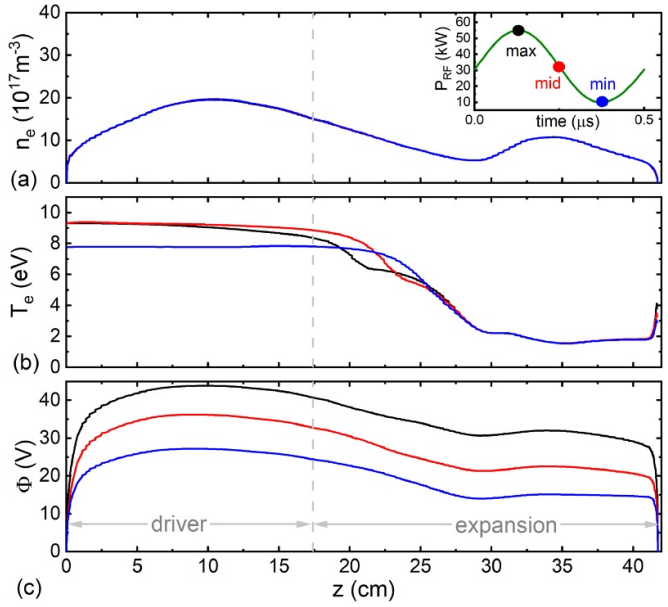

Figure 5. The axial (from the middle of the driver backplate to the middle of the PG) oscillation of the electron density (a), the electron temperature (b) and the plasma potential (c) at the maximum (the black curves), in the middle (the red curves) and in the minimum (the blue curves) of the P_{RF} period, obtained at the same discharge conditions as figure 4.

small changes in the strength and the orientation of $\mathbf{\Gamma}_e$. At the minimum of the P_{RF} oscillation appears a high (by absolute value) negative potential of −80 V (figure 6(c)) in the region close to the coil, which changes the structure of the electron flux in the expansion region. The region with −80 V forms a strong electric field for the electrons and, in combination with the $\mathbf{B}_{RF}$, leads to a strong increase of the Lorentz Force over the other terms in (4), resulting in a robust increase of the upstream $\mathbf{\Gamma}_e$. In addition, with the further shift of the entire axial Φ profile to lower values (figure 5(c), the blue curve), the second vortex disappears, resulting in a higher $\mathbf{\Gamma}_e$ to PG with reversed orientation. In this particular moment of the P_{RF} time period, the electron current (I_e) collected from the PG (figure 7 the black curve) increases 5 times: from ∼4 A to ∼20 A.

3.2. Simplified model

The averaged over the RF period power deposition profile is obtained from the RF self-consistent model according to (12) and it is exported in the simplified model (figure 8) as an input parameter. Figure 9 shows the spatial distribution of the plasma parameters obtained from the simplified model. In both the same MFF profile is applied (figure 2(b)), causing $\mathbf{\Gamma}_e$ in the simplified mode (figure 9(a) the arrow plot) with a similar vortex-type structure and orientation as the one in the full model (figure 4(a)), particularly in the expansion. Furthermore, I_e collected by the PG shows close values in both models: 9 A from the simplified model and 9.4 A time averaged over 1 RF period from the self-consistent model (figure 7 the green and grey curves). Identical to the full model, n_e in the simplified one has two maxima (figure 9(a)). Since the RF coil is not accounted for, the non-linear effects such as the ponderomotive and the RF Lorentz forces are not present and thus do not limit $\mathbf{\Gamma}_e$ close to the side walls of the driver (in the region of the coil), resulting in a non-squeezed profile of n_e. The spatial distribution of Φ has two maxima (figure 9(b)) similar to the full model (figure 4(b)); however, the maximum in the driver is more localised in the middle (but it is not symmetric) of the driver, due to the absence of x component of the electric field. The electron temperature in the driver is between 11 eV and 12 eV in the simplified model (figure 9(c)), while these high values of T_e for the self-consistent model are in the region close to the wall next to the coil (figure 4(c)) followed by a decrease towards the center of the driver. However, in both models, T_e decreases rapidly in axial direction through the MFF, reaching values of (1–2) eV in front of the PG. From the comparison of the models, it is visible that the main difference in the results is in the driver, while in the extraction region, the plasma parameters as well as $\mathbf{\Gamma}_e$ are similar.

For a more comprehensive analysis, the results from the models are compared on a vertical line, 2 cm away from the PG. Both models show the same behaviour of n_e (figure 10(a)): a bigger and wider maximum located in the top-middle region and a smaller maximum in the bottom. The simplified model gives 8×10^{17} m^{-3} in the first maximum and 4.2×10^{17} m^{-3} in the second one, while the RF self-consistent model gives 7×10^{17} m^{-3} and 5.1×10^{17} m^{-3} in the first and the second

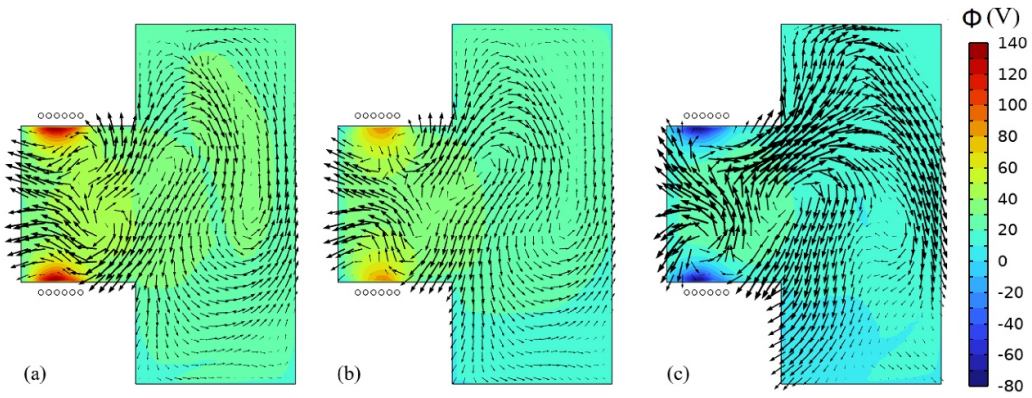

Figure 6. The change of spatial distribution of the plasma potential and the electron flux with the arrows over an RF cycle: in the maximum (a), in the middle (b) and in the minimum (c) of P_{RF} period, obtained at the same source parameters as figure 4.

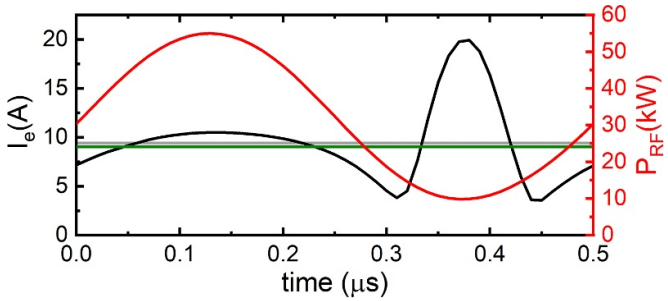

Figure 7. The change of the I_e on the PG (the black curve) during one P_{RF} period (the red curve) together with the time-averaged I_e obtained from the RF self-consistent model (the grey curve) and I_e from the simplified model (the green curve).

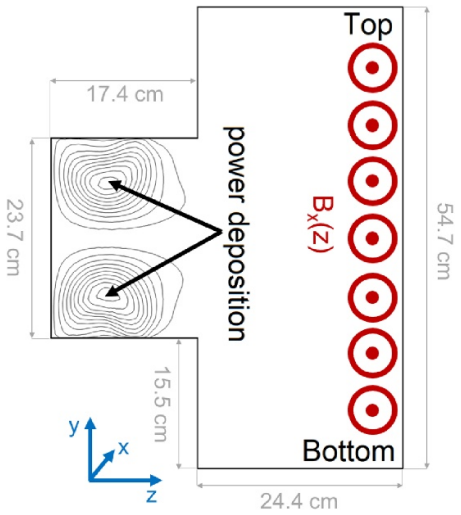

Figure 8. The modelling domain and the power deposition profile for the simplified model.

maxima, respectively. The plasma potential (figure 10(b)) is with higher values on top, ∼20 V for the simplified model and ∼21 V for the full one, while on the bottom side the difference in Φ values is larger with the highest difference of 2.5 V: 17.5 V for the simplified model and 15 V for the full model. The simplified model gives a more uniform Φ profile. The electron temperature (figure 10(c)) follows the same behaviour for both models: higher T_e in the vicinity of the walls due to electron losses on the surfaces, 3 eV on the top and (4–5) eV on the bottom, and almost constant values of ∼2 eV in the plasma bulk. The simplified model provides a smoother T_e vertical profile. The major difference is in the vicinity of the bottom expansion side wall, where T_e deviates by 42% for both models: 5 eV in the full model and 3.5 eV in the simplified model.

The comparison shows that both models give similar and close results for the plasma parameters and the electron flux in the extraction region, as well as for the electron current collected by the PG. Therefore, to study in detail the effects of biasing surfaces away from the driver, it is sufficient to use a simplified model with a power deposition profile set as an input parameter.

4. Results for ELISE geometry

4.1. Modelling domain

The ion source at the ELISE test facility has four drivers arranged two by two and a common expansion chamber [13]. The modelling domain (figure 11(a)) is a 2D vertical planar plane taken in the middle of two drivers (one top and one bottom) with the actual size of the source. Since ELISE has drivers with bigger radii (13.8 cm) than BUG (11.85 cm) and uses a different topology of the MFF (figure 11(b)), at first, the RF self-consistent model is computed for a geometry with one ELISE size driver to obtain $P_{ind}(y, z)$. Subsequently, the power deposition profile is set as an input parameter for each driver in the ELISE modelling domain. The results in this chapter are at 0.3 Pa, 60 kW per driver and MFF with an axial profile as shown in figure 11(b) generated by high current (1.5 kA) flowing through the PG with 22 G at the maximum and being used for daily ELISE operation. The wall potential is set to 0 V except for the bias on the PG and BP, which will be varied in the course of the study. For this purpose, the

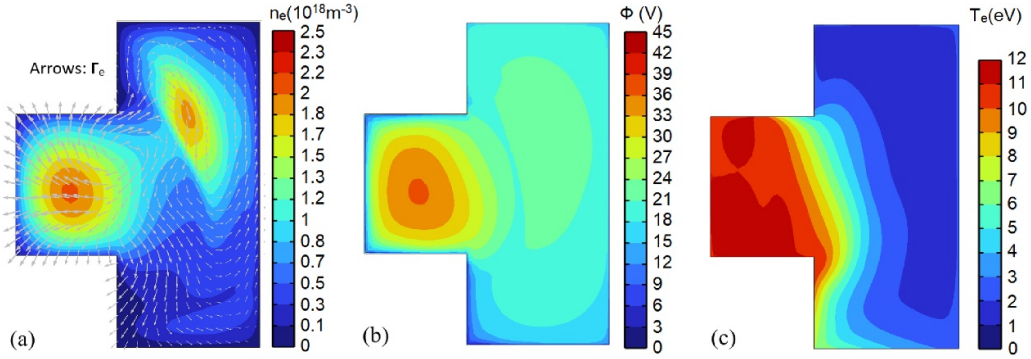

Figure 9. The same as figure 4 but for a model without taking into account the RF coil and with imported power deposition profile.

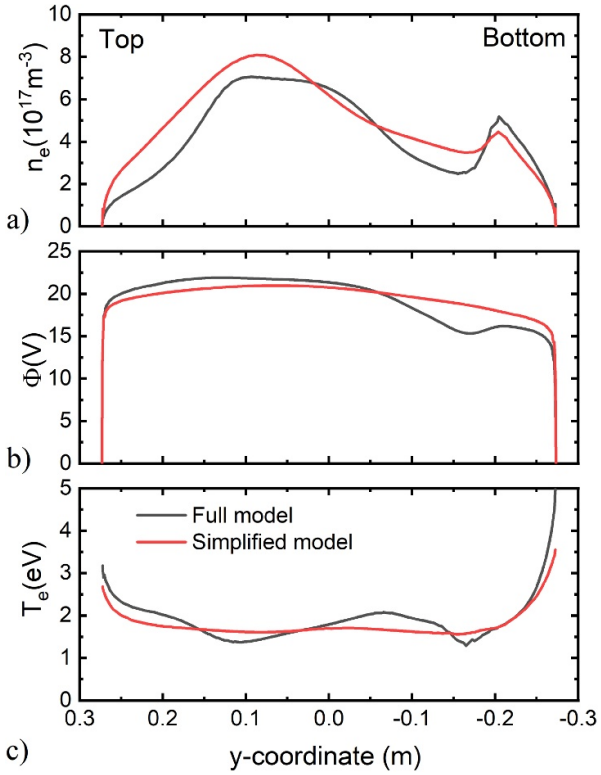

Figure 10. Comparison of the RF self-consistent (black curves) and simplified (red curves) models at a vertical line, 2 cm away from the PG for the electron density (a), plasma potential (b) and electron temperature (c). Coordinate $y = 0$ m indicates the middle of the PG, positive values of y-coordinate are the top area of the source and the negative ones respectively the bottom.

rightmost boundary of the modelling domain (at the end of the expansion) is split into different sections corresponding to PG and BP as indicated in figure 11(a) with their actual vertical lengths. With this procedure, the boundary conditions for the Poisson equation (3) can be varied separately for PG and BP.

Furthermore, the model applied to ELISE is expanded with surface-produced negative ions. They are treated as electrons with the proton mass and emission rate corresponding to 200 Am^{-2}, which seems to be realistic [30] and set as a boundary condition on the PG and BP surfaces. The emission rate value is a rough estimation from n_a and a surface conversion of an atom to a negative ion rate $\sim$0.3, depending on the negative ion temperature [31]. The volume production of the negative ions is not included in the model.

4.2. Results and discussions

To illustrate the effect of PG and BP biases on the plasma parameters first, chapter 4.2.1 presents the results for the spatial distributions of n_e, T_e, Φ, as well as $\mathbf{\Gamma}_e$ in a configuration of PG and BP on the source wall potential, i.e. 0 V and in the presence of MFF. After that, the next chapter 4.2.2 shows the results with applied potentials to the PG and BP simultaneously and the introduced changes of the discharge structure.

4.2.1. Spatial distribution of the plasma parameters with MFF.

The electron flux (figure 12(a) the arrow plot) has a vortex-type structure, similar to results with BUG geometry. The diamagnetic drift ($\nabla(n_e T_e)$) induces vortexes at the exit of

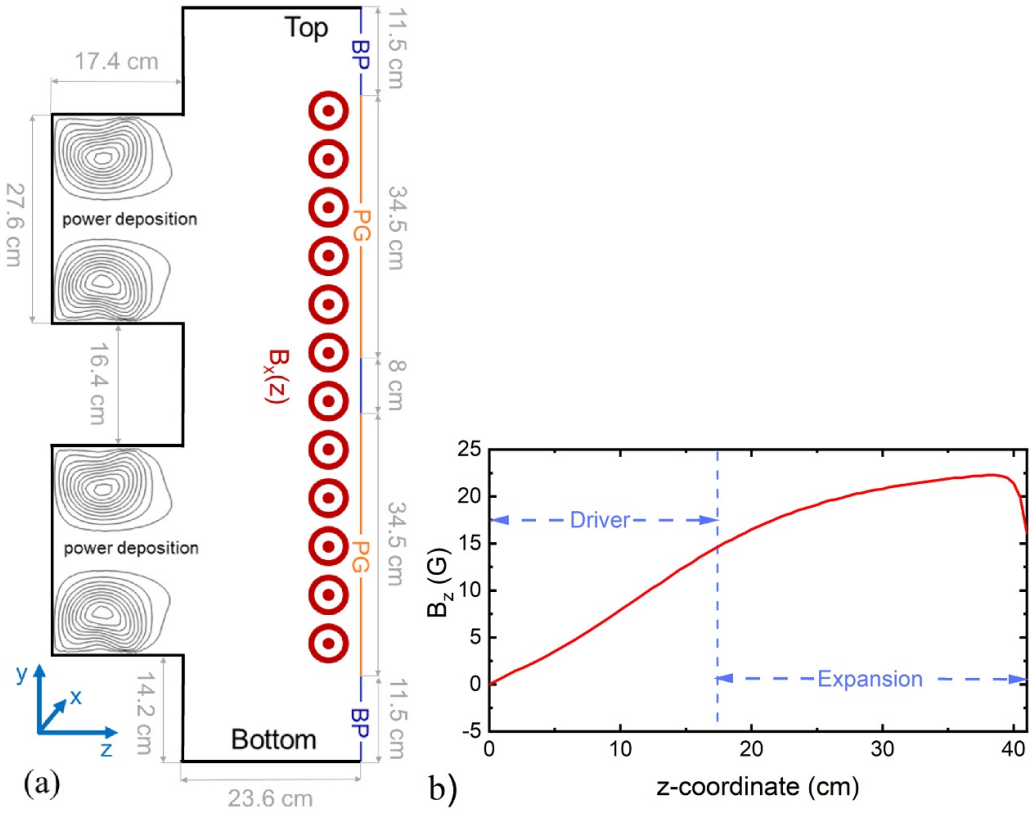

Figure 11. ELISE modelling domain (a) and the axial profile MFF used in the experiments (b) generated by high current flowing through PG ($I_{\mathbf{PG}} = 1.5$ kA).

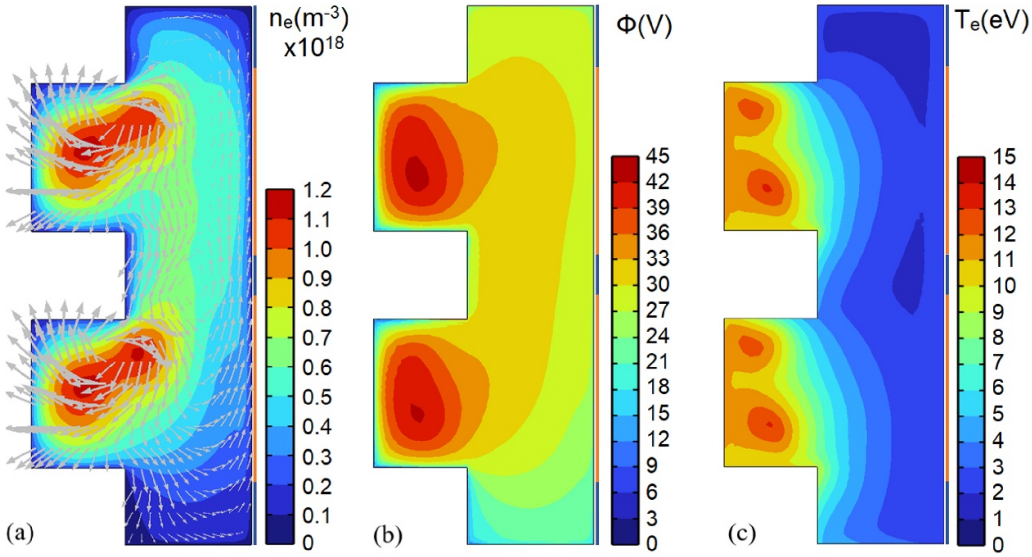

Figure 12. The spatial distribution of the electron density together with its flux as an arrow plot (a), plasma potential (b) and the electron density (c) at ELISE with MFF, 0.3 Pa, 60 kW per driver and $U_{\mathrm{PG}} = 0$ V and $U_{\mathrm{BP}} = 0$ V. The location of the PG (in orange) and the BP (in blue) is shown at the end of the modelling domain on the right.

every driver (figure 12(a) the arrow plot), which result in an accumulation of second n_e maxima approximately in the middle of their loops, while the first n_e maxima remain in the drivers. The vortex associated with the $\mathbf{E} \times \mathbf{B}_{\mathrm{FF}}$ drift enlarges over the entire vertical length of the expansion chamber. It defines the orientation of $\mathbf{\Gamma}_e$ in the vicinity of the PG and the BP—similar to BUG. Furthermore, $\mathbf{E} \times \mathbf{B}_{\mathrm{FF}}$ drift carries electrons from top to bottom close to the backplate between the drivers. This results in a plateau with increased values between the drivers in the n_e spatial distribution and a higher second maximum of the electron density at the bottom.

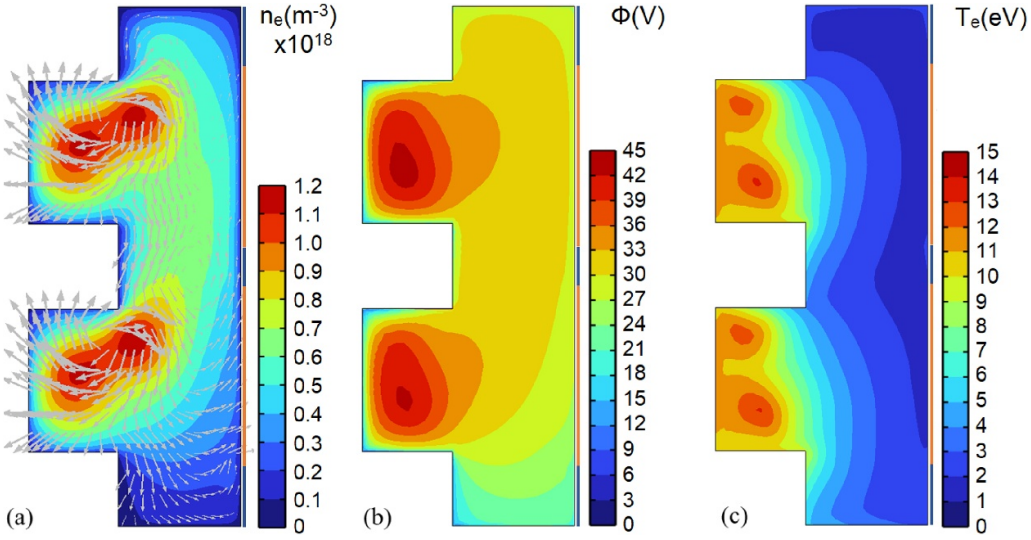

Figure 13. The same as figure 12 but for $U_{\mathrm{PG}} = 20$ V and $U_{\mathrm{BP}} = 0$ V.

The plasma potential (figure 12(b)) has maxima in the drivers and decreases in an axial direction towards the PG, as it does in [32]. In the region between the drivers, Φ follows n_{e} spatial distribution due to $\mathbf{\Gamma}_{\mathrm{e}}$ and the Boltzmann relation, i.e. the formation of a plateau in the area between the top and bottom drivers.

The highest values of T_{e} are locked in the drivers (figure 12(c)), with two maxima in each driver approximately in the middle of the power deposition profile (figure 11(a)), next to every side wall. Since the used axial profile of the MFF provides higher values of the magnetic field in the drivers (figure 11(b)) compared to BUG, it more strongly affects the electron thermal flux. This is responsible for the electron temperature as well as the electron density and the plasma potential asymmetry in the drivers. As a result, T_{e} maxima in each driver is strongly localised with a higher maximum downstream in each driver.

4.2.2. Effect of the PG and BP bias on the plasma parameters. In the experiments at ELISE, the PG and the BP are biased by the current applied to the respective surfaces. In this way the potential is self-consistently defined and it depends on the gas-discharge conditions such as gas pressure, RF power, MFF strength, etc. For example, in the source parameters used in this study, a set current on the PG (I_{bias}) with a value of 5 A, defines a potential (U_{PG}) at approximately 20 V in a case of BP (U_{BP}) is on a source wall potential, i.e. $U_{\mathrm{BP}} = 0$ V. The size of the PG to the other walls is large enough (with a ratio in the modelling domain $R_{\mathrm{PG}} = L_{\mathrm{PG}}/(L_{\mathrm{walls}} + L_{\mathrm{BP}}) \sim 0.28$), thus by increasing U_{PG}, the plasma potential profile (figure 13(b)) shifts to higher values, particularly in the expansion with up to 2 V, due to potential locking [26]:

$$\Phi = U_{\mathrm{PG}} - \frac{T_{\mathrm{e}}}{e} \ln \left[\frac{\sqrt{\mu(1+R_{\mathrm{PG}})}}{R_{\mathrm{PG}} + \exp\left(-eU_{\mathrm{PG}}/T_{\mathrm{e}}\right)} \right], \qquad (13)$$

where $\mu = \sqrt{2.3 m_{\mathbf{e}}/m_{\mathbf{i}}}$ with $m_{\mathbf{i}}$ is the mass of the positive ions. The plasma parameters in the drivers show minor changes compared to the results in section 4.2.1. In the expansion, the increased values of Φ shift the vortex associated with the $\mathbf{E} \times \mathbf{B}_{\mathrm{FF}}$ drift towards the PG (figure 13(a) the arrow plot), resulting in increased n_{e} in front of the PG. In addition, biasing the PG changes the orientation and the strength of $\mathbf{\Gamma}_{\mathrm{e}}$ in the vicinity of the PG. On the bottom side, the electron flux is oriented towards the PG segment, and on the top $\mathbf{\Gamma}_{\mathrm{e}}$ is significantly decreased. Varying U_{PG} step-wise from $(0-25)$ V affects the potential difference $\Delta U_{\mathrm{PG}} = \Phi - U_{\mathrm{PG}}$ in front of the PG—ΔU_{PG} goes from 30 V to 10 V on top and from 25 V to 6 V on the bottom. This reduction of ΔU_{PG} results in an increase of I_{e} collected from the PG (figure 15(a), the orange symbols), defined as integration of the electron boundary conditions on the surface. In addition, $U_{\mathrm{PG}} =$ 20 V decreases T_{e} in the vicinity of the extraction region (figure 13(c)).

In ELISE experiments with BP on a $U_{\mathrm{BP}} \neq 0$ V, the plate is set with a floating potential or biased via a set current I_{BP}, the latter defines a bias above the floating potential. In addition, in the modelling domain, the size of the BP is smaller than the PG. However, this is not true for experiments where the surface of the BP (0.528 m^2) is approximately 1.5 times larger than the PG surface (0.345 m^2). Therefore, by biasing the BP, Φ shifts to higher values, together with U_{PG} (PG bias being defined by a set I_{bias}). Furthermore, in the experiments, U_{BP} never exceeds U_{PG}, thus modelling-wise U_{BP} is set to 18 V while $U_{\mathrm{PG}} = 20$ V.

Applying the potential on the BP $U_{\mathrm{BP}} = 18$ V introduces minor changes in the spatial distribution of the plasma parameters (figure 14 plots only for n_{e} with $\mathbf{\Gamma}_{\mathrm{e}}$). However, the BP potential difference $\Delta U_{\mathrm{BP}} = \Phi - U_{\mathrm{BP}}$ decreases to 13 V near the top segment and to 8 V near the bottom one and the orientation of $\mathbf{\Gamma}_{\mathrm{e}}$ (figure 14(b) the arrow plot) changes, particularly in the vicinity of the bottom BP surfaces.

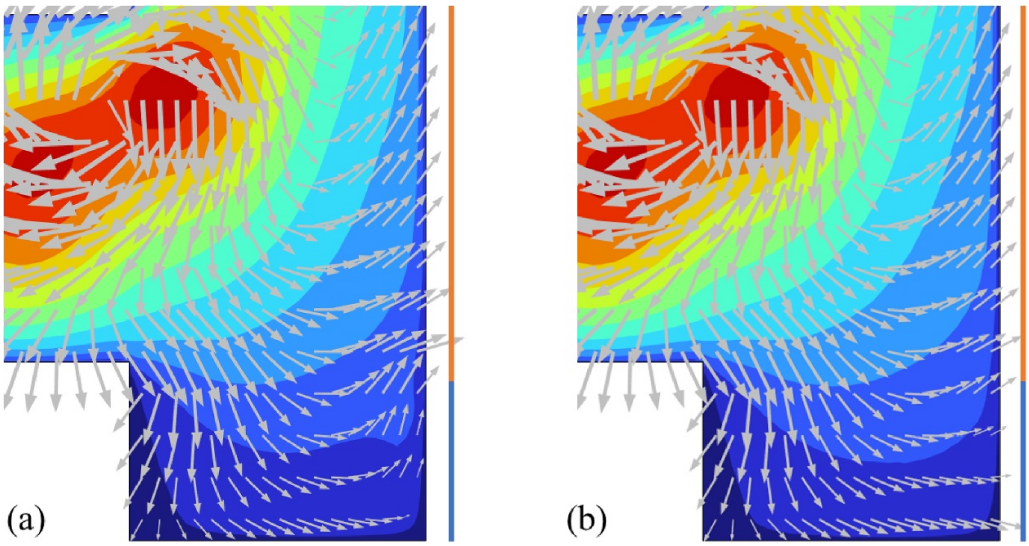

Figure 14. Zoomed plots of n_e spatial distribution and $\mathbf{\Gamma}_e$ with the arrows on the bottom part of the source in cases of $U_{PG} = 20$ V, $U_{BP} = 0$ V (a) and $U_{PG} = 20$ V, $U_{BP} = 18$ V (b).

The total collected current (I_{BP}) by the bottom part of the BP (ion and electron boundary conditions integrated over the surface) decreases (from 2 to −3.5 A) and even have negative values (figure 15(b)), while on the top it remains positive and almost constant (3 A). The negative I_{BP} on the bottom segment indicates that more electrons are collected than positive ions. In addition, in figure 15(a), the green symbols show a decrease in the electron current collected by the PG with the increase of U_{BP}. This can be interpreted as part of the electrons carried by $\mathbf{\Gamma}_e$ are collected by BP before being collected by the PG surface or extracted, therefore, the co-extracted electron current can be reduced.

In the experiments, the I_{BP} and the co-extracted electron current on the EG can be measured individually on the top and bottom grid segments at the ELISE ion source. The comparison of the experimentally obtained BP currents (figure 15(c)) with those obtained from the model (figure 15(b)) shows different absolute values due to the model taking into account a 2D cut of the source, however, the results show similar trends: the measured I_{BP} on the bottom segment, becomes negative by setting the BP from the source wall potential (at $U_{BP} = 0$ V) to floating potential ($U_{BP} = 22.5$ V, via set $I_{BP,set} \approx 0$ A and the sum of the measured top and bottom current on the BP is equal to the set value of $I_{BP,set}$), while the current on top segment remains positive with a slight decrease. When applying more positive potential to the BP, more electrons are collected by the BP surface, resulting in more negative I_{BP} on the bottom, similar to the modelling results (figure 15(b)) with smaller values on the top. The co-extracted electron currents (figure 15(d)) decrease by two times by setting the BP from the source wall potential to floating potential: from 4.7 to 2.1 A on the bottom and from 3.5to 1.24 A on the top. This confirms the statement that applying a potential to the BP collects part of the electrons before the extraction via changing the potential difference (ΔU_{PG} and ΔU_{BP}) and the orientation of $\mathbf{\Gamma}_e$ in the vicinity of the extraction region.

4.2.3. Surface-produced hydrogen negative ions. The surface-produced negative ions are emitted from surfaces with a low work function (1.4 eV or less). For this purpose, a small fraction of caesium [33] vapour is released in the ion source, providing a layer with a low work function on the walls. However, the electron affinity of the negative ions is 0.75 eV [34] and the dominant mechanism for their loss is collisions with electrons and mutual neutralisation. In these conditions, the mean free path of the negative ions ranges from less than 1 cm in the drivers to 5 cm in the expansion. This means that the negative ion density (n_n) in the regions with high T_e would be negligible. Therefore, it is chosen in the model that the surface produced negative ions are emitted from the PG and the BP, where the main caesium accumulation would be.

The surface-produced negative ions experience an accelerating electric field towards the plasma bulk due to the potential drop in the wall region, the negative ion flux ($\mathbf{\Gamma}_n$) is oriented towards the region of high Φ (figure 16(a) the arrow plot). In combination, with the low electron affinity, the formation of n_n maximum is in a region with low T_e, as it is in the case of PG and BP in the source potential ($U_{PG} = U_{BP} = 0$ V) (figure 16(a)): n_n maximum located on the top half of the source, in front of the PG. Biasing the PG with $U_{PG} = 20$ V ($U_{BP} = 0$ V) provides an extended maximum of n_n towards the bottom side of the source (figure 16(b)), which is a result of the decreased T_e (figure 13(c)) and the increase of Φ (figure 13(b)) in front of the PG. Applying a potential of $U_{BP} = 18$ V to the BP further extends the negative ion density towards the bottom part, resulting in a more homogeneous distribution of the negative ions in the vertical direction in front of the PG and the BP.

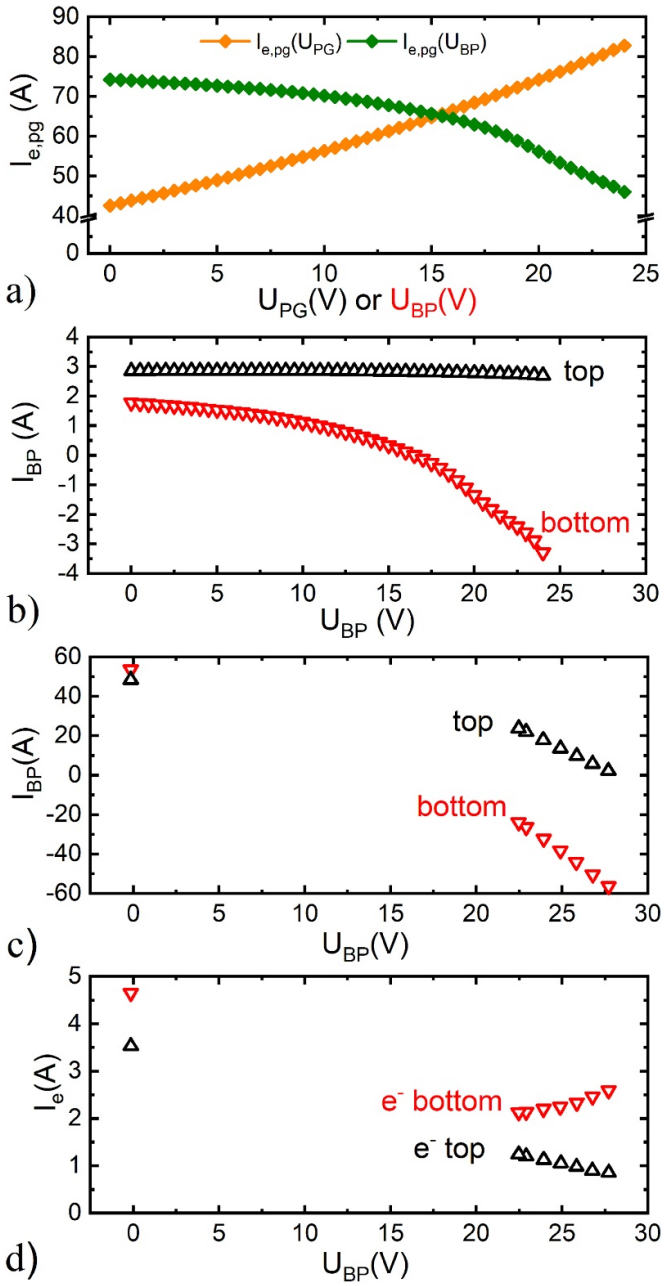

Figure 15. Currents obtained from the model: change of the electron current collected by PG with the increase of U_{PG} at BP on source wall potential $U_{BP} = 0$ V (in orange); and U_{BP} sweep at $U_{PG} = 20\,V$ (in green) (a) and the total current collected by the top (in black) and the bottom (in red) BP segments as a function of U_{BP} sweep (b). Experimental results: for the change of BP current on the top (in black) and on the bottom (in red) segments with U_{BP} (c), as well as the change of the co-extracted electrons on top (the black), on the bottom (in red).

The fluid modelling cannot account for the extracted negative ions, where the majority are extracted directly from the PG surface [35] without entering the plasma. In addition, the fluid model cannot resolve the real plasma sheath and the influence of the virtual cathode studied from the ONYX calculations [35] on the penetration of the negative ions cannot be taken into account. Nonetheless, the fluid model gives very valuable insights into biasing with and without negative ions present in the expansion region. Nevertheless, in reality, there is also an extraction of negative ions from the plasma bulk and the vertically symmetric n_n profile at biased PG and BP can improve the extracted negative ion beam uniformity.

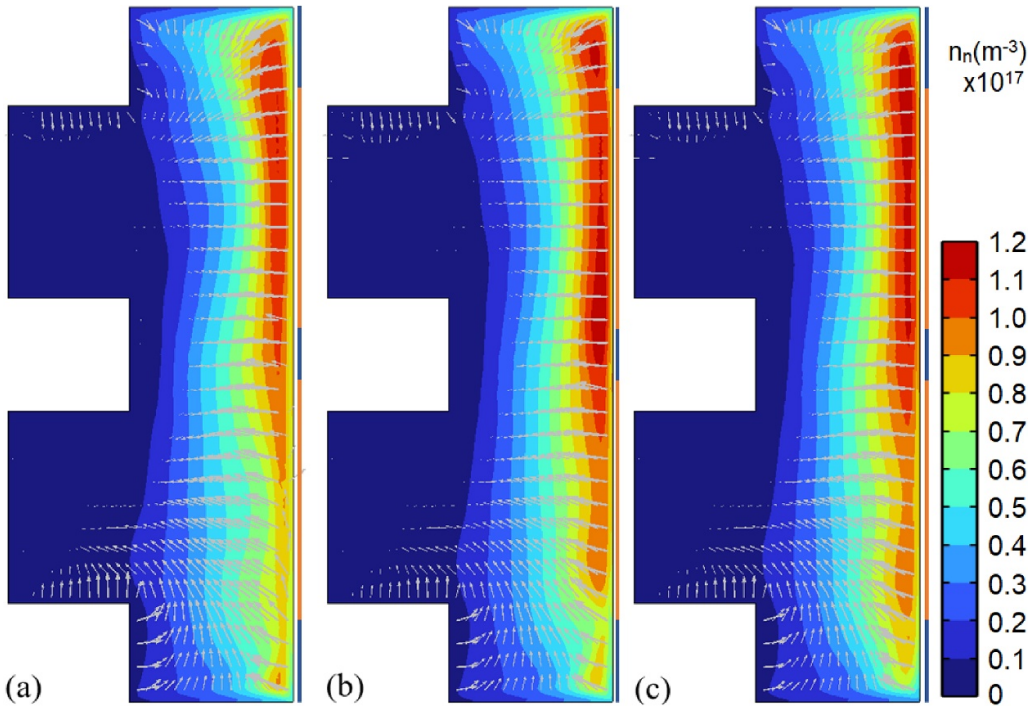

Figure 16. Spatial distribution of the negative ions at $U_{PG} = 0$ V and $U_{BP} = 0$ V (a), $U_{PG} = 20$ V and $U_{BP} = 0$ V (b) and $U_{PG} = 20$ V and $U_{BP} = 18$ V (c).

5. Summary

A 2D fluid plasma model is applied to the prototype ELISE negative hydrogen/deuterium ion source for NBI. The goal is to investigate the effect of biasing PG and BP surfaces in combination with an MFF on the plasma parameters in the vicinity of the extraction as a means to reduce the co-extracted electrons. However, a proper model accounting for the dynamics of the neutrals and electrodynamic equations for the RF coil can be a time-consuming and computation-demanding problem in a large modelling domain. In addition, the study requires bias variations of two different surfaces, which would increase the computational effort tremendously. Therefore, the model is simplified by not taking into account the electrodynamics of the RF coil but setting a power deposition profile as an input parameter. This procedure provides fewer degrees of freedom and, respectively, accelerates the model with a computational time of several hours instead of 30 or more hours for one run. The simplified model is applied to a smaller modelling domain for the BUG ion source. The results are compared with those from a well-known and benchmarked RF self-consistent model for the same domain and gas-discharge conditions. The results in the region of interest, in the expansion of the source, reasonably agree, which gives evidence to apply the simplified model to the ELISE ion source.

The RF self-consistent model of the BUG geometry shows the change of the plasma parameters within the P_{RF} period. The fluctuation of the plasma potential, in combination with the magnetic field from the filter, affects the electron flux and the electron current on the PG at the minimum of the oscillation. In this particular moment of the RF power cycle, the Lorentz force increases tremendously, sending a robust flux towards the PG and the collected electron current from the PG surface increases from 4 to 20 A for 1 μs.

However, the simplified model cannot resolve the RF cycle; therefore, for comparison purposes of both models, the results from the self-consistent one are averaged over the RF frequency period. The results for the n_e, T_e, Φ and $\mathbf{\Gamma}_e$ from both models show differences in the driver due to non-linear effects induced by the coil, i.e. the RF Lorentz and the ponderomotive forces. However, the plasma parameters have similar values for both models in the expansion chamber in front of the extraction region, as well as for the electron currents collected by the PG. This gives confidence to apply the simplified model to the ELISE geometry, where the area of interest of the study is, namely, in the expansion close to the extraction region.

Applying a bias of 20 V on the PG while other walls are at 0 V, including the BP at the ELISE ion source, changes the discharge structure in the vicinity of the extraction region. When the PG size is large enough, its bias shifts the plasma potential by up to 2 V to higher values due to the potential locking. The higher Φ in the expansion moves the vortex associated with $\mathbf{E} \times \mathbf{B}$ drift in the electron flux towards the PG, resulting in a higher and more homogeneous electron density in the vertical direction. The difference in the plasma and PG potentials decreases to 10 V on top and to 6 V on the bottom, allowing more electrons to be collected

by the PG surface, particularly on the bottom side of the ion source.

Biasing the BP with 18 V while the applied potential to the PG is 20 V introduces minor changes in the plasma parameters due to the smaller size of the PG in the 2D modelling domain. However, the BP potential affects the electron flux by changing its orientation and strength in the vicinity of its surface. The potential sweep of the BP shows that the collected current decreases and even becomes negative on the bottom segment of the plate, which is in agreement with the experimental results. The negative current indicates that the collected electrons are more than the collected positive ions. Furthermore, the bias of the BP reduces the electron current collected by the PG as well as the experimentally measured co-extracted electrons. In conclusion, applying a bias to the BP changes the electron flux in the vicinity of the extraction system, resulting in a collection of electrons on the surface prior to the extraction and reduction of the co-extracted electron current by more than two times. Biasing of the PG and BP provides a more homogeneous profile of the negative ions in the vertical direction in the vicinity of the extraction beamlet groups, which can benefit the negative ion beam with better convergence.

Data availability statement

The data that support the findings of this study are available upon reasonable request from the authors. The results presented in the paper are based on very specific input parameters (e.g. cross sections, pressure, magnetic field, potentials and etc). As such, any requests for output data should be addressed to the authors directly to ensure appropriate context and use.

Acknowledgments

This work has been carried out within the framework of the EUROfusion Consortium, funded by the European Union via the Euratom Research and Training Programme (Grant Agreement No 101052200 – EUROfusion). Views and opinions expressed are however those of the author(s) only and do not necessarily reflect those of the European Union or the European Commission. Neither the European Union nor the European Commission can be held responsible for them.

ORCID iDs

D Yordanov 0000-0001-5522-5301
D Wünderlich 0000-0003-2810-9633
C Wimmer 0000-0003-4691-4265
U Fantz 0000-0003-2239-3477
D Zielke 0000-0003-4231-4350

References

[1] Lieberman M A and Lichtenberg A J 2005 *Principles of Plasma Discharges and Materials Processing* (Wiley)
[2] Muramatsu M and Kitagawa A 2012 *Rev. Sci. Instrum.* **83** 02B909
[3] Spädtke P, Bossler J, Emig H, Leible K, Mühle C, Schulte H and Tinschert K 1998 *Nucl. Inst. Methods Phys. Res. B* **139** 145–9
[4] Hopf C, Starnella G, den Harder N and Fantz U 2021 *Nucl. Fusion* **61** 106032
[5] Hemsworth R S and *et al* 2017 *New J. Phys.* **19** 025005
[6] Singh M J, Boilson D, Polevoi A R, Oikawa T and Mitteau R 2017 *New J. Phys.* **19** 055004
[7] Berkner K, Pyle R and Stearns J 1975 *Nucl. Fusion* **15** 249
[8] Speth E and *et al* 2006 *Nucl. Fusion* **46** S220–38
[9] Bacal M 2006 *Nucl. Fusion* **46** S250–9
[10] Boeuf J P, Chaudhury B and Garrigues L 2012 *Phys. Plasmas* **19** 113509
[11] Lishev S, Schiesko L, Wünderlich D, Wimmer C and Fantz U 2018 *Plasma Sources Sci. Technol.* **27** 125008
[12] Toigo V *et al* 2017 *New J. Phys.* **19** 085004
[13] Heinemann B and *et al* 2017 *New J. Phys.* **19** 015001
[14] Wünderlich D and *et al* 2019 *Nucl. Fusion* **59** 084001
[15] Wimmer C and Fantz U 2016 *J. Appl. Phys.* **120** 073301
[16] Fubiani G and Boeuf J P 2013 *Phys. Plasmas* **20** 113511
[17] Yordanov D, Wunderlich D, Wimmer C and Fantz U 2022 *J. Phys.: Conf. Ser.* **2244** 012050
[18] Fantz U *et al* 2022 *J. Phys.: Conf. Ser.* **2244** 012049
[19] Zielke D, Rauner D, Briefi S, Lishev S and Fantz U 2021 *Plasma Sources Sci. Technol.* **30** 065011
[20] Zielke D, Briefi S, Lishev S and Fantz U 2022 *Plasma Sources Sci. Technol.* **31** 035019
[21] Kolev S, Lishev S, Shivarova A, Tarnev K and Wilhelm R 2007 *Plasma Phys. Control. Fusion* **49** 1349
[22] Hagelaar G J M, Fubiani G and Boeuf J P 2011 *Plasma Sources Sci. Technol.* **20** 015001
[23] Boeuf J P, Hagelaar G J M, Sarrailh P, Fubiani G and Kohen N 2011 *Plasma Sources Sci. Technol.* **20** 015002
[24] Wünderlich D, Montellano I M, Lindqvist M, Mimo A, Mochalskyy S and Fantz U 2021 *J. Appl. Phys.* **130** 053303
[25] Yordanov D, Lishev S and Shivarova A 2016 *J. Appl. Phys.* **119** 183302
[26] Baalrud S D, Scheiner B, Yee B T, Hopkins M M and Barnat E 2020 *Plasma Sources Sci. Technol.* **29** 053001
[27] Janev R K Reiter D and Samm U 2003 Forschungszentrum Jülich, Zentralbibliothek
[28] Briefi S and Fantz U and the NNBI Team 2018 *AIP Conf. Proc.* **2052** 040005
[29] Fubiani G and Boeuf J P 2014 *Phys. Plasmas* **21** 073512
[30] Mochalskyy S, Wünderlich D, Fantz U, Franzen P and Minea T 2015 *Nucl. Fusion* **55** 033011
[31] Fubiani G, Garrigues L, Hagelaar G, Kohen N and Boeuf J P 2017 *New J. Phys.* **19** 015002
[32] Boeuf J P, Claustre J, Chaudhury B and Fubiani G 2012 *Phys. Plasmas* **19** 113510
[33] Belchenko Y I and Davydenko V I 2006 *Rev. Sci. Instrum.* **77** 03B702
[34] Middleton R 1989 *A Negative Ion Cookbook* (University of Pennsylvania)
[35] Mochalskyy S, Fantz U, Wünderlich D and Minea T 2016 *Nucl. Fusion* **56** 106025